Accepted Manuscript

"A realistic projection simulator for laboratory based X-ray micro-CT"

Jelle Dhaene, Elin Pauwels, Thomas De Schryver, Amelie De Muynck, Manuel Dierick, Luc Van Hoorebeke

DOI: doi:10.1016/j.nimb.2014.09.033

Published in: *Nuclear Instruments and Methods in Physics Research Section B: Beam Interactions with Materials and Atoms*

Received date: 6 June 2014
Accepted date: 26 September 2014

Please cite this article as:
J. Dhaene, E. Pauwels, T. De Schryver, A. De Muynck, M. Dierick and L. Van Hoorebeke
Nuclear Instruments and Methods in Physics Research Section B: Beam Interactions with Materials and Atoms; **342**, p. 170-178

A realistic projection simulator for laboratory based X-ray micro-CT

Jelle Dhaene[1a], Elin Pauwels[a], Thomas De Schryver[a], Amelie De Muynck[a], Manuel Dierick[a], Luc Van Hoorebeke[a]

[a] *Ghent University, UGCT - Dept. Physics and Astronomy*
Proeftuinstraat 86; B-9000 Gent, Belgium

Abstract

In X-ray Computed Tomography (CT) each voxel of the reconstructed image contains a calculated grey value which represents the linear attenuation coefficient for the materials in that voxel. Conventional laboratory based CT scanners use polychromatic X-ray sources and integrating detectors with an energy dependent efficiency. Consequently the reconstructed attenuation coefficients will depend on the spectrum of the source and the spectral sensitivity of the detector. Beam hardening will alter the spectrum significantly as the beam propagates through the sample. Therefore, sample composition and shape will affect the reconstructed attenuation coefficients as well.
A polychromatic projection simulator has been developed at the "Centre for X-ray Tomography" of the Ghent University (UGCT) which takes into account the aforementioned variables, allowing for complete and realistic simulations of CT scans for a wide range of geometrical setups. Monte Carlo simulations of the X-ray tubes and detectors were performed to model their spectral behaviour. In this paper, the implementation and features of the program are discussed. Simulated and real CT scans are compared to demonstrate the quantitative correctness of the simulations. Experiments performed at two different UGCT scanners yield a maximum deviation of 3.9% and 6.5% respectively, between the measured and simulated reconstructed attenuation coefficients.

Keywords: Computed Tomography, Simulation, Polychromatic, X-rays

[1]Corresponding authors: E-mail jelle.dhaene@ugent.be; elin.pauwels@ugent.be Tel. +32 9264 6532 Fax +32 9264 6697

1. Introduction

The "Centre for X-ray Tomography" of the Ghent University (UGCT; `www.ugct.ugent.be`) is a research facility specialised in high resolution X-ray computed tomography (CT). Currently 4 complementary state-of-the-art micro-CT scanners have been built at UGCT, two of which reach a spatial resolution well below 1 micrometer [1, 2, 3].
At UGCT a large variety of samples, both in terms of size and composition, is scanned for a wide range of applications. To optimise image contrast, ideal scanning conditions have to be created which will be different for each sample. Therefore, realistic simulations which take into account the influence of various scanning variables, such as emitted spectrum by the source, detector response characteristics, beam filtration and the sample itself, can be very useful to define the optimal scanner settings [4].
Several research groups have developed a simulation tool for X-ray imaging for different purposes, e.g. VXI [5, 6, 7, 8, 9], XRayImagingSimulator [10, 11, 12], ScorpiusXLab [13], XRSIM [14], etc. However, most of these tools are developed in-house to meet specific needs for their own research and are not readily available. Furthermore, thorough experimental quantitative comparisons with real CT scans are often not presented in literature. The intent at UGCT is to have a flexible, fast and accurate simulation tool which can be used in a routine way to test and define optimal scanner settings and which has been tested for its quantitative correctness by comparing real and simulated CT scans. Therefore, a GPU based program - Arion - has been developed to simulate radiographic projections, incorporating the physical aspects and limitations of laboratory based X-ray micro-CT.
The result of a CT scan is a virtual 3D representation of the sample composed of voxels. Each voxel contains a calculated grey value which represents the linear attenuation coefficient for the materials in that voxel. This linear attenuation coefficient is the product of the local density and mass attenuation coefficient, the latter being dependent on both the chemical element(s) present and the incident photon energy. Conventional laboratory based CT scanners use X-ray sources producing a polychromatic spectrum, in combination with integrating detectors with an energy dependent efficiency. The transmitted monochromatic intensity through the sample $I(E)$ is given by the Lambert-Beer law:

$$I(E) = I_0(E)exp(-\mu(E)d), \tag{1}$$

with $I_0(E)$ the intensity of the photon beam emitted by the X-ray source, $\mu(E)$ the linear attenuation coefficient, d the sample thickness and E the monochromatic photon energy. This law is used in reconstruction algorithms. Consequently, the actually measured grey values in the voxels will depend on the incident X-ray spectrum and the spectral sensitivity of the detector. The polychromaticity will also induce effects such as metal artefacts and beam hardening, characterised by an upward shift of the average energy of the beam while it propagates through the sample. Therefore, also sample size, shape, elemental composition and density will have a significant influence on the resulting grey values. All these variables are taken into account in the simulation tool.

To model the polychromatic behaviour of source and detector, Monte Carlo simulations were performed for each X-ray tube and detector available at UGCT. The radiographic projections are computed using a ray-tracing technique which determines the total attenuation in a ray. The X-ray spectrum is divided into energy bins and for each detector pixel the contribution from each energy bin can be added, yielding a polychromatic projection image.

Arion is a stand-alone application, written in C++. The program is very flexible, allowing for instance to choose a wide range of geometrical setups. For every component - source, sample and detector - a position and orientation for every projection can be defined. Conventional CT setups such as circular and helical CT scans are readily available. A conveyer belt has been implemented as well, but also other (industrial) setups can be defined by the user and used for the simulations.

In this paper, Arion and its physical background is presented and thoroughly tested for its quantitative correctness. First, the general structure of the program and the Monte Carlo simulation of the sources and detectors will be discussed in section 2. In section 3, the physical background of the program will be explained. Finally, in section 4 simulated and experimental CT data will be compared.

2. Material and Methods

Figure 1 shows a flowchart of the different steps during the setup of a CT scan simulation with Arion, illustrating the general structure of the program. These steps are implemented in a single graphical user interface (GUI).

The program includes several other tools in addition to the projection simulator itself, such as a material creator, phantom creator and Setup Optimiser.

The material creator tool allows the user to generate the attenuation data for molecules, mixtures, such as concrete, soft tissue, etc. and solutions based on the mass fractions of the constituent elements. This data can then be used in the simulator. With the phantom creator a slice or stack of slices can be loaded to produce a phantom sample file which can be accessed during the scan setup. The Setup Optimiser uses functions of the projection simulator to evaluate the influence of different scanner settings in a straightforward way. After selecting a specific X-ray tube, tube voltage, beam filtration and detector type, the detected transmission of the polychromatic X-ray beam through a material or combination of materials can be calculated. Furthermore, several parameters of the emitted and detected spectrum are computed, as well as a measure for the expected amount of beam hardening.
For accurate simulations of a CT scan, the polychromatic behaviour for every component - source, sample and detector - has to be known. How this data is obtained will be discussed in this section.

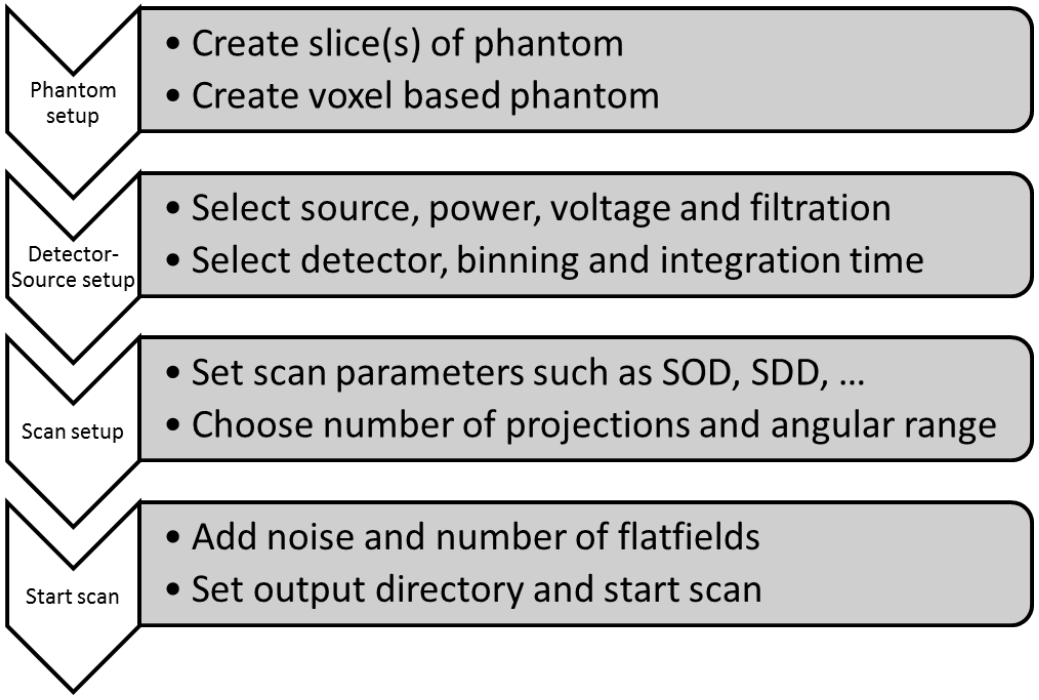

Figure 1: Flowchart of the different processes during a CT scan simulation.

2.1. Simulation of source and detector

For each type of X-ray tube and detector the polychromatic behaviour will differ according to their composition and design. For example, the entrance window and scintillator thickness will have a significant influence on the spectral sensitivity of a detector. So the polychromatic aspect of each available X-ray source and detector at UGCT has to be characterised separately. To achieve this, Monte Carlo simulations were performed using BEAMnrc (`www.nrc-cnrc.gc.ca/eng/solutions/advisory/beam_index.html`), taking into account the geometrical design of each specific component (Fig. 2). As a result, detailed but non-negligible effects such as for example the production of secondary radiation [15] in a transmission-type X-ray tube (see below), are included in the obtained data. Photon cross sections were imported from the XCOM Photon Cross Sections Database from NIST (`www.nist.gov`).

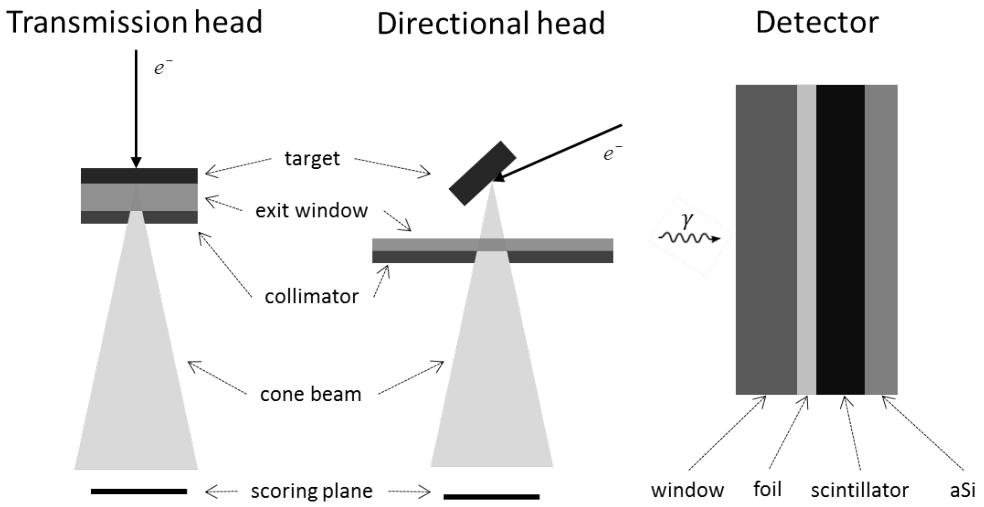

Figure 2: (a) Schematic representation of a transmission (left) and directional head (right) of an X-ray tube. Target, exit window and collimator are indicated. (b) Schematic representation of the different layers inside a flat panel detector. Note that the thicknesses of the layers are not in proportion.

2.1.1. Source

Inside an X-ray tube, electrons are emitted from a hot filament and accelerated towards a target, usually tungsten. The electrons are focused using

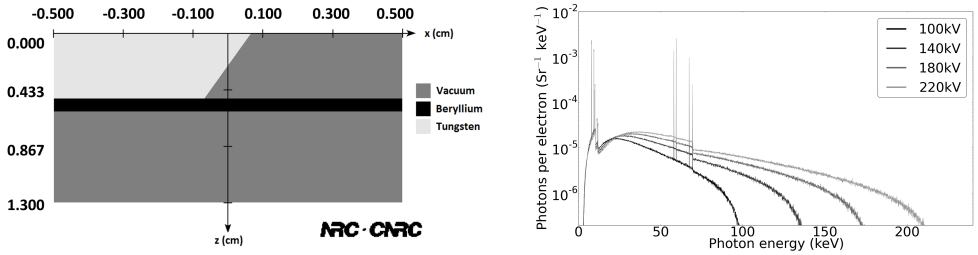

(a) (b)

Figure 3: (a) Geometry of a directional X-ray tube as used for the Monte Carlo simulations with BEAMnrc. (b) Simulated spectra for a directional tube. The number of photons per Sr per simulated electron per keV is given as a function of photon energy. The bin width of the histogram is 50 eV.

electromagnetic lenses. There are 2 main types of X-ray tubes as can be seen in figure 2(a). In a directional tube the electron beam impinges on the target at a fixed angle and due to a collimator X-ray photons are emitted from the tube only at an angle of typically 60° to 90° relative to the incident direction of the electrons. In a transmission tube the electrons impinges perpendicular onto a target which is thin enough to allow the X-ray photons to pass through the target and leave it on the opposite side.

To determine the generated energy spectra, Monte Carlo simulations are used since these are more accurate than tabulated semi-empirical data [16, 17, 18, 19, 20]. Moreover, the internal structure of the X-ray tube can be taken into account, which is important for contributions such as secondary radiation. The interactions of the electrons are simulated and the path and energy of the produced photons are calculated. The paths of the emitted photons are traced while moving through the exit window (and optional collimator) towards a square scoring plane of 1 cm^2 at a distance of 5 cm which corresponds to a typical solid angle covered by the detector in micro-CT. All photons crossing this plane are tallied. The solid angle covered by the scoring plane $\Delta\Omega_{source}$ is given by [21]:

$$\Delta\Omega_{source} = 4\, arccos\left(\sqrt{\frac{1+2\alpha^2}{(1+\alpha^2)^2}}\right) = 0.0396\, Sr, \tag{2}$$

with $\alpha = a/2d$ where a is the length of the side of the square scoring plane and d the distance of the plane to the source. The number of photons per energy bin in this solid angle is counted. As such, a spectrum can be generated for

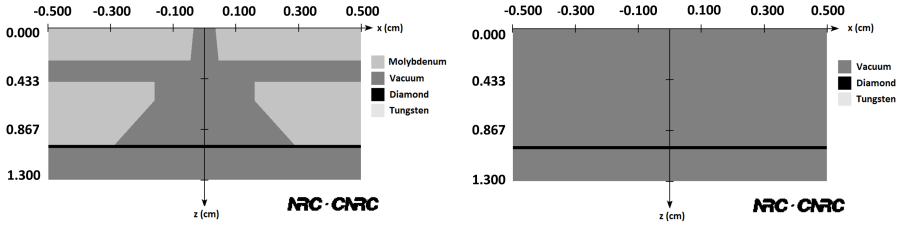

(a)

(b)

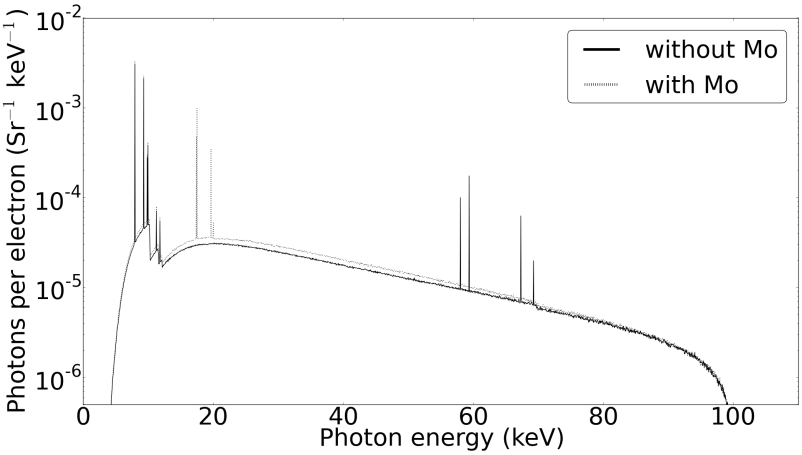

(c)

Figure 4: Geometry of the Feinfocus FXE160.51 transmission head with (a) and without (b) Mo structures, used for the Monte Carlo simulations with BEAMnrc. Note that the thin tungsten target is not visible on the diamond backing. (c) Simulated spectra with and without Mo structures. Note the additional peaks originating from the Mo structures.

a given X-ray tube and voltage. Figure 3(a) shows the geometry used for the Monte Carlo simulation with BEAMnrc for a directional tube. Figure 3(b) shows the simulated spectra.

Table 1: Integrated spectra for the transmission tube simulated with and without Mo structures.

Tube	Integrated spectrum (photons per electron per Sr)
without Mo	1.6276×10^{-3}
with Mo	1.9183×10^{-3}

Especially for a transmission tube, the internal structure has to be taken into account for the simulations. One of the X-ray tubes used at UGCT is a Feinfocus X-ray tube with FXE160.51 transmission head, which contains molybdenum (Mo) structures for the walls of the vacuum chamber and the aperture. Electrons which are backscattered from the target and X-ray photons emitted from the rear of the target can give rise to bremsstrahlung and characteristic radiation when hitting these Mo structures. This is called secondary radiation [15]. The influence of this contribution was investigated by performing a Monte Carlo simulation for the same transmission tube with and without the Mo structures. Figure 4 shows the geometry used in BEAMnrc and the generated spectra. Integration of the spectra shows that 17.85% more photons per electron are generated if the Mo is taken into account (Table 1). It is therefore important to include these structures in the simulation.

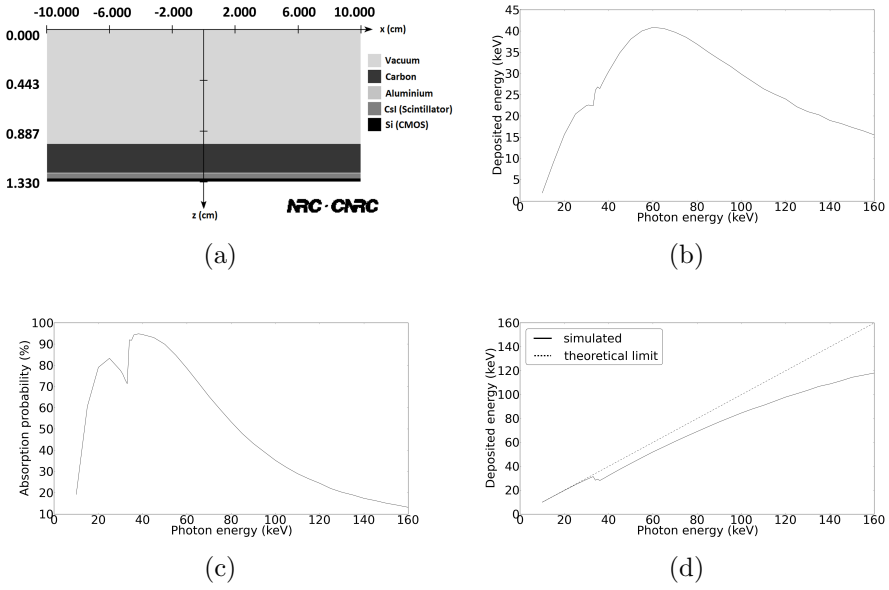

Figure 5: (a) Geometry of a detector used for the Monte Carlo simulations with BEAMnrc. From the simulations the mean deposited energy per incident photon (b) and the absorption probability of a photon (c) can be calculated. Dividing (b) by (c) yields the mean deposited energy per interacting photon (d).

2.1.2. Detector

A typical flat panel detector is composed of an entrance window (1) usually made of carbon, a thin aluminium foil (2), a scintillator (3) and an amorphous silicon (aSi) detector layer (4) as seen in figure 2(b). The foil is added to reflect all visible photons created and emitted by the scintillator in the direction of the entrance window towards the detector layer. The scintillator is usually made of caesium iodide (CsI) grown in a columnar structure. The number of counts per pixel in a radiographic projection is proportional to the deposited energy of the X-rays in the scintillator in front of the pixel, while we assume that the noise in the image depends on the amount of X-ray photons detected per pixel. For accurate simulations these two detector characteristics have to be taken into account.
Using BEAMnrc the spectral sensitivity of the detector can be simulated. The interactions of a beam of mono-energetic photons emitted onto a predefined detector geometry (Fig. 5(a)) are traced which allows to calculate the deposited energy in the scintillator (Fig. 5(b)) and the actual number of interacting X-ray photons (Fig. 5(c)) as a function of energy.

2.2. Sample

Elemental tabulated attenuation data for the materials contained in the sample and filters were obtained from the XCOM Photon Cross Sections Database from NIST.
The sample is built up from a stacked sequence of image files (that can be interpreted as RGB format internally), each representing a single slice in a 3D voxel based volume. As such, a segmented reconstructed dataset of a real CT scan can be loaded for testing under several scan conditions. Different colours in the bitmaps represent different materials which can be assigned to each voxel during the sample building. The attenuation data for each element up to atomic number 100 (Fm) is included in Arion. To simulate a radiographic projection, the total linear attenuation coefficient is used. The various contributions to the total attenuation coefficient - photo-electric absorption, Compton and Rayleigh scattering - are also calculated, which allows to study these effects separately as well.

2.3. Scan geometry

One of the features of Arion is the flexibility in defining a scan geometry. Consequently it can be used to simulate standard circular and helical CT scans but more exotic and industrial CT setups, where limitations with

regard to angular range and number of projections have to be taken into account, can be modeled as well. For every projection the position and rotation of source, sample and detector can be defined, allowing to create every possible CT setup. The position component consists of 3 coordinates (x,y,z), while the rotation component consists of a skew, tilt and slant which are rotations around the x-, y- and z-axis respectively. In the predefined setups (circular, helical, conveyer belt) these coordinates are automatically calculated, based on a few user defined input parameters. The circular CT setup for instance requires only a given source-object distance (SOD) and source-detector distance (SDD).

3. Calculation

Simulation of the radiographic projections is essentially based on the Lambert-Beer law (1). Since both the intensity of the X-ray beam and the linear attenuation coefficient are dependent on the photon energy, (1) can be rewritten as follows:

$$I = \sum_{i=1}^{n} I_{0,i} exp(-\mu_i d), \tag{3}$$

with n the number of energy bins used, $I_{0,i}$ the intensity of the emitted photon beam in energy bin i and μ_i the linear attenuation coefficient for energy bin i. For each energy bin and pixel a ray-tracing technique is applied to calculate the total attenuation of the ray along the path from source to detector. The resulting number of photons N_i along a ray for energy bin i is given by:

$$N_i = N_{0,i} exp(-\sum_{j=1}^{m} \mu_{i,j} d_j), \tag{4}$$

with $N_{0,i}$ the initial number of photons in energy bin i, m the number of materials in the sample crossed by the traced ray, $\mu_{i,j}$ the linear attenuation coefficient of material j in energy bin i and d_j the thickness of material j crossed by the ray. The number of detected photons in energy bin i, $N_{d,i}$, is the product of (4) with the detector efficiency for energy bin i, $D_{eff,i}$:

$$N_{d,i} = D_{eff,i} \times N_i. \tag{5}$$

Since this is equal to the amount of photons detected in a detector pixel for energy bin i, the noise in the image can be calculated with this value assuming

Poisson statistics. The standard deviation on the number of detected photons in an energy bin $\sigma_{N_{d,i}}$ is given by the square root of (5):

$$\sigma_{N_{d,i}} = \sqrt{N_{d,i}}. \tag{6}$$

The total detected energy E_d per pixel is given by:

$$E_d = \sum_{i=1}^{n} E_{d,i} = \sum_{i=1}^{n} D_{d,i} N_{d,i}, \tag{7}$$

with $E_{d,i}$ the detected energy per pixel for energy bin i and $D_{d,i}$ the mean deposited energy per interacting photon in energy bin i. For a large number of photons (more than 20) in an energy bin, we assume a gaussian error propagation. Thus the standard deviation on (7), σ_{E_d}, can be calculated as follows:

$$\sigma_{E_d} = \sqrt{\sum_{i=1}^{n} \left(\sigma_{E_{d,i}}\right)^2} = \sqrt{\sum_{i=1}^{n} \left(D_{d,i}\sigma_{N_{d,i}}\right)^2}, \tag{8}$$

with $\sigma_{E_{d,i}}$ the standard deviation on the detected energy per pixel for energy bin i.
The number of photons for energy bin i emitted in the solid angle of a pixel $\Delta\Omega_{pixel}$ (see section 3.1), $N_{emitted\ photons,i}$, is given by:

$$N_{emitted\ photons,i} = \left(\frac{P\Delta t}{UQ_{e^-}}\right)(\Delta\Omega_{pixel}\Delta E_i S'_i). \tag{9}$$

The first factor, $\frac{P\Delta t}{UQ_{e^-}}$, equals the amount of electrons accelerated in the tube during exposure. In this expression represents P the tube power, Δt the integration time, U the tube voltage and Q_{e^-} the elementary charge. The second factor contains the width of an energy bin ΔE_i, the solid angle of the pixel $\Delta\Omega_{pixel}$ and the filtered spectrum S'_i, expressed as the number of photons per simulated electron per Sr per keV (see section 3.2).
Using (4) and (5) the number of photons for energy bin i detected in a pixel can be calculated as follows:

$$N_{d,i} = \frac{P\Delta t}{UQ_{e^-}}\Delta\Omega_{pixel}\Delta E_i S'_i D_{eff,i} exp(-\sum_{j=1}^{m}\mu_{ij}d_j). \tag{10}$$

3.1. Solid angle of a pixel

The solid angle of a pixel $\Delta\Omega_{pixel}$ takes into account the distance between the pixel and the source r and the orientation of the pixel. Let $\mathbf{n}$ be the normal vector on the plane of the pixel and $\mathbf{u}$ the normalised vector that defines the direction from source to pixel. The solid angle of the pixel with pitch a can be written as:

$$\Delta\Omega_{pixel} \approx \frac{a^2 \mathbf{n} \cdot \mathbf{u}}{r^2} = \frac{a^2 cos(\theta)}{r^2}, \tag{11}$$

with θ the angle between the 2 vectors.

3.2. Beam filtration

Multiple filters can be added in the scan setup of the simulator. Before the actual simulation starts, the X-ray spectrum is modified as follows:

$$S'_i = S_i \prod_{j=1}^{l} exp(-\mu_{ij} d_j), \tag{12}$$

with l the number of added filters and S'_i and S_i representing the filtered and unfiltered spectrum respectively, both expressed as the number of photons per simulated electron per Sr per keV.

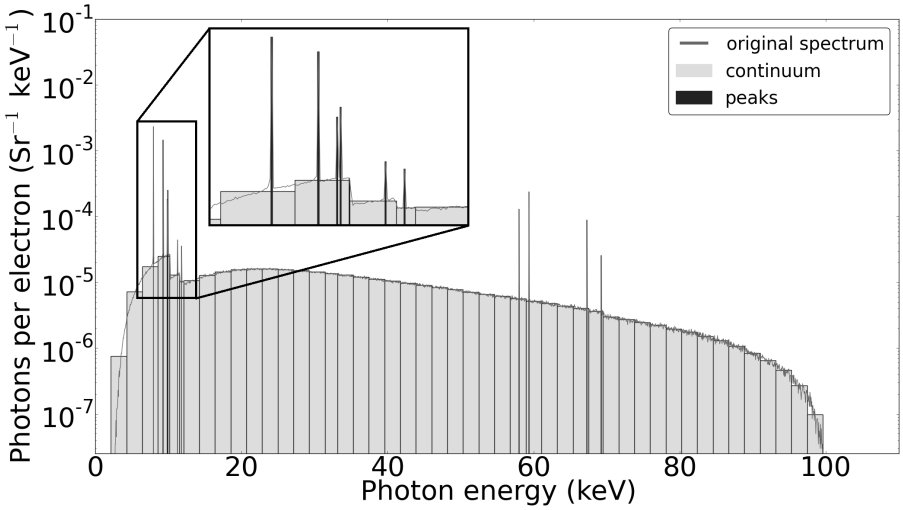

Figure 6: Example of a binned spectrum resulting in a reduction of the number of energy bins by a factor of 20. Note that the bin width is not constant.

3.3. Binning of the X-ray spectra

The previously shown spectra are subdivided into energy bins of 50 eV. This energy resolution is sufficiently small to model the peaks originating from characteristic radiation in the spectrum. The continuum on the other hand can be reproduced accurately by using a larger bin size. As such, the number of energy bins can be reduced resulting in significantly shorter computation times. In figure 6 an example of a binned spectrum is shown, where the number of bins (and therefore the computation time) is reduced by a factor of 20. Notice that not all energy bins have the same width, which has to be incorporated in (10). During the rebinning process all edges (K and L) of target material, filtration, sample materials and scintillator are taken into account, to preserve the shape of the spectrum as good as possible.

3.4. Spotsize of the source

The spot created inside the target by the accelerated electrons from which the photons are emitted in an X-ray tube has a certain dimension which is called the spot size and wich will impose a limit on the achievable resolution in the reconstructed volume. The relation between the geometrical unsharpness U_G, as defined in figure 7, and the focal spot size F of a projected image is given by:

$$U_G = F(m-1), \tag{13}$$

with m the magnification, which is defined as the ratio of SDD to SOD. To obtain a sharp projection, the geometrical unsharpness has to be smaller than the detector pixel size p. The resolution of the reconstructed volume in case of a point source is given by $R = p/m$. Taking a finite focal spot size into account, the achievable resolution becomes:

$$R = p/m + F(1 - 1/m), \tag{14}$$

which results in $R \approx F$ for large magnification as is the case in micro-CT. Typically, scan parameters are chosen to ensure that geometrical unsharpness becomes negligible and the source can be considered as a point source. Therefore, geometrical unsharpness has not yet been included in the simulation program for now.

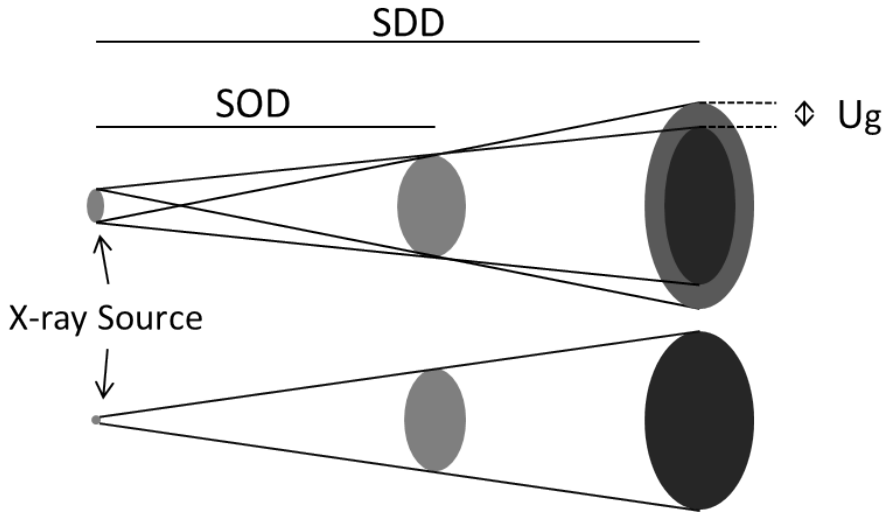

Figure 7: Influence of the focal spot size on the resulting image. U_G is the geometrical unsharpness, SDD and SOD are the source-detector and source-object distance.

4. Results and Discussion

The experiments described below were performed at two different UGCT scanners. First, transmission values through several filters in a real radiographic projection are compared with simulated projections. Subsequently, reconstructed attenuation coefficients of a real and simulated CT scan are compared and an example is shown to illustrate the possibility to model beam hardening. Finally, some benchmarks and future improvements will be listed. Scanning parameters in the following experiments are chosen to match optimal scanning conditions in terms of detector range and image quality.

4.1. Comparison of transmission values

The conversion of deposited energy in a pixel to the number of counts in that pixel is slightly dependent on the energy of the X-rays. However, this behaviour depends on the scintillator thickness, electronics and gain factor of the detector and will here be treated as a constant factor. Taking this into account, the transmission T through a material can be written as follows:

$$T = \frac{E}{E_0}, \tag{15}$$

with E and E_0 the total detected energy in a pixel with and without the material present in the X-ray beam as defined by (7). The standard deviation on the transmission σ_T is given by:

$$\sigma_T = \frac{1}{E_0}\sqrt{\sigma_E^2 + \frac{E^2}{E_0^2}\sigma_{E_0}^2}, \tag{16}$$

with σ_E and σ_{E_0} the standard deviations on E and E_0.
Table 2 shows the measured and simulated transmission values through several filters with varying thickness. The filters were placed immediately after the source covering the whole X-ray beam. Projection images of 512 by 512 pixels were obtained. The measurements were performed at the Nanowood scanner [3] at a tube voltage of 120 kV and a power of 3.6 W. The detector distance was 663.1 mm and an integration time of 2 s was used. The standard deviations on the real data σ_M and the simulation σ_S are not the standard deviations on the measured and simulated transmission but are determined based on the inter-pixel variation and using (16), respectively. The deviations listed are the relative differences between the real and simulated data. Comparing simulated and real data proves that Poisson statistics are a good approximation to model the noise in the images.

Table 2: Measured(M) and simulated(S) transmission values and corresponding standard deviations(σ_M and σ_S) at 120 keV. Deviations(Dev) between real and simulated data are listed as well.

Filter	M(%)	S(%)	Dev(%)	σ_M(%)	σ_S(%)
50 μm W	42.3	41.6	-1.7	0.42	0.46
30 μm Mo	70.6	69.3	-1.8	0.55	0.63
150 μm Al	95.5	95.6	0.1	0.34	0.77
68 μm Cu	70.8	71.9	1.6	0.74	0.65
136 μm Cu	58.0	59.0	1.7	0.72	0.58
272 μm Cu	43.7	44.0	0.7	0.61	0.48
544 μm Cu	28.8	28.5	-1.0	0.48	0.38

Figure 8(a) shows a projection image of an Al sphere (6 mm diameter) taken at the micro-CT scanner described in [1]. Figure 8(b) shows the effect of the secondary spot on the projection image. A custom collimator can be mounted on the tube to reduce the effect of the secondary spot and a line profile of such projection is compared with the line profile of a simulated projection (Fig. 9). During the simulation only the spectrum produced by

the target (and not the Mo) was taken into account. The SOD and SDD of the scan were 102.8 and 862.8 mm, respectively, at a tube voltage of 100 kV and a power of 10 W. Projection images of 910 by 725 pixels with a resolution of 30 μm were obtained. Again can be concluded that the predicted and measured transmissions are in good agreement. The mean reason for the difference is that the secondary spot is not completely removed by using the custom collimator.

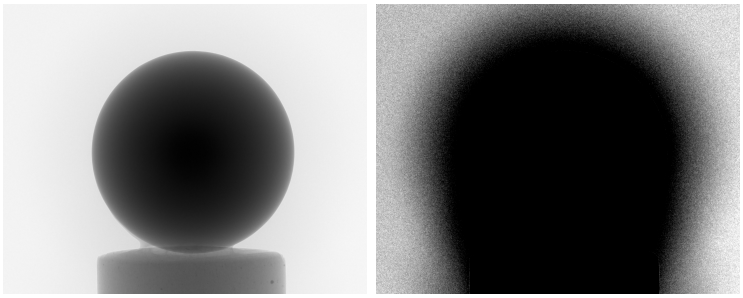

(a) (b)

Figure 8: A radiographic projection (a) and the halo created by the secondary spot of the tube (b). (Both images are generated using the same projection but another grey value scaling is used.)

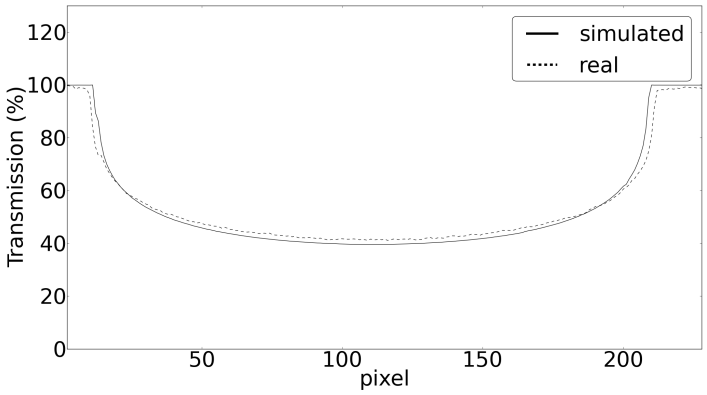

Figure 9: Line profile of a real and a simulated radiographic projection.

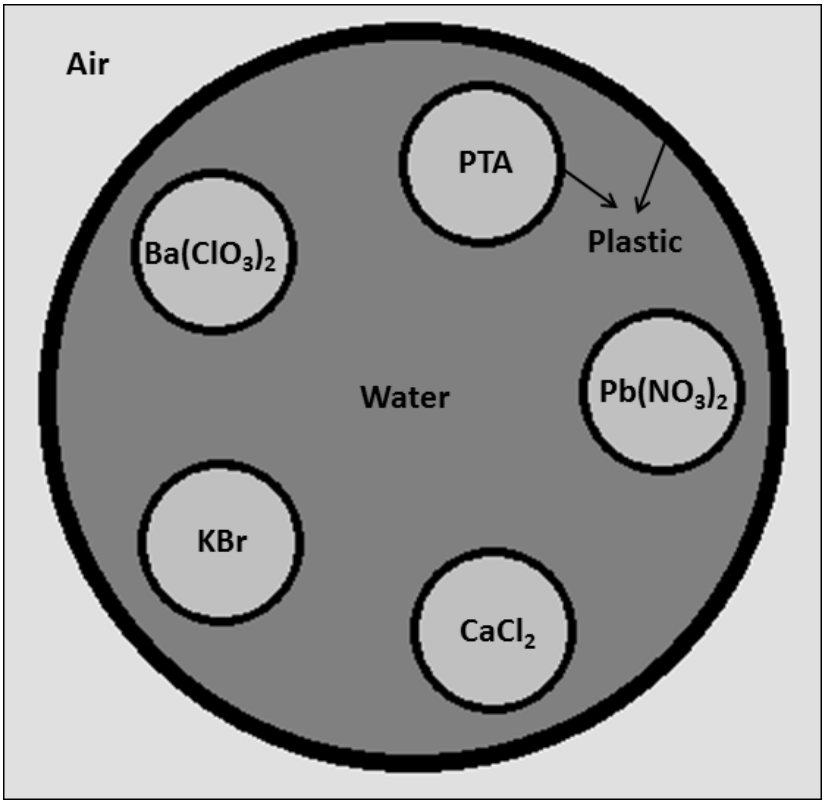

Figure 10: Model of the phantom used for the comparison between real and simulated CT scans.

4.2. Comparison of reconstructions

A cylindrical phantom filled with water and containing five tubes with different aqueous solutions - barium chlorate, potassium bromide, calcium chloride, lead nitrate and phosphotungstic acid (PTA) - of known concentration was used for comparison (Fig. 10 and Table 3). The scans were performed at the Nanowood scanner [3] with a directional microfocus X-ray tube (Hamamatsu L9181), operated at 100 kV, and a Varian 2520V Paxscan aSi flat panel detector. The SOD and SDD were 287.6 and 689.9 mm, respectively, resulting in a voxel size of 105 μm. An aluminium filter of 0.45 mm thickness was used for beam filtration. The tube power was set to 16 W and an integration time of 0.8 s per projection was chosen. Reconstruction of the projection data was done with Octopus (`www.octopusreconstruction.com`) [22], a software package developed at UGCT, using the algorithm of Feldkamp, Davis and

Table 3: Mass fractions of the solutes and water and the density for each solution used in the phantom (Fig. 10).

Material	Mass fraction solute	Mass fraction H_2O	density (g/cm^3)
$Ba(ClO_3)_2$	0.103	0.897	1.115
KBr	0.115	0.885	1.13
$CaCl_2$	0.412	0.588	1.32
$Pb(NO_3)_2$	0.078	0.922	1.085
PTA	0.074	0.926	1.08

Kress (FDK) [23].
Figure 11 shows reconstructed slices of the real and simulated CT scan of the phantom. No beam hardening correction was applied during the reconstruction to compare both reconstructions in a proper manner. Note that the beam hardening artefacts, which are typical features resulting from the use of polychromatic X-ray spectra, are well reproduced by the simulation.
In table 4 the reconstructed attenuation coefficients for the materials present in the phantom are compared. The maximum deviation observed between the real and simulated reconstructed attenuation coefficients is 3.9% for the $CaCl_2$ solution. However, due to the high concentration of this solution (41.2% mass fraction), its density is not known with good accuracy. Therefore, this uncertainty on the density may also play a role in the relatively large deviation for the $CaCl_2$ solution. Nevertheless the results demonstrate the quantitative correctness of the simulations both for the measured reconstructed attenuation coefficients and for the noise in the reconstructions.
A similar experiment was performed at the scanner described in [1] and a maximum deviation of 6.5% was observed. Note that, as previously mentioned, the effect of the secondary spot can have an influence on the result.

4.3. Modeling beam hardening

The Al sphere (Fig. 8) can also be used to evaluate the changes of the spectrum as it propagates through the sample. The reconstructed attenuation coefficients will be drastically lower in the middle of such a phantom due to beam hardening. The sphere was scanned with and without the custom collimator, applying the same scan parameters as used for the radiographic projections in section 8(a). The scan resulted in a voxel size of 30 μm. Figure 12(b) shows a line profile of a reconstruction of the scan without the collimator. The effect of the secondary spot is clearly visible. Figure 12(c)

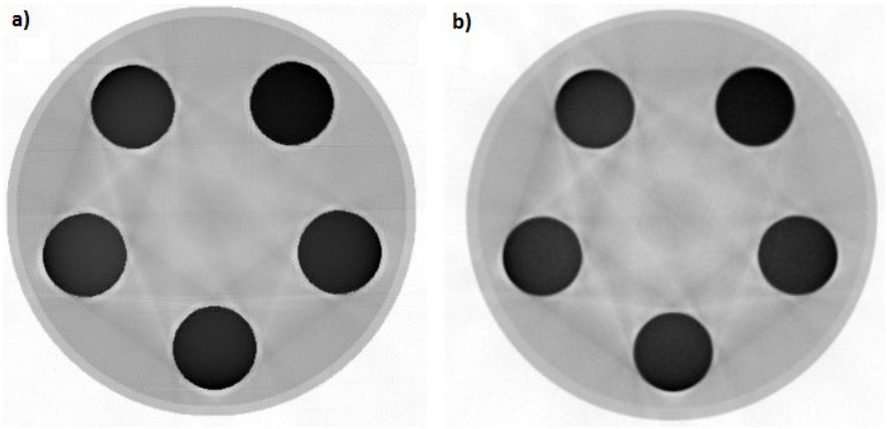

Figure 11: Reconstructed slice of the simulated (a) and real (b) CT scan.

Table 4: Measured(M) and simulated(S) reconstructed attenuation values and corresponding standard deviations(σ_M and σ_S) at 100 keV for the different materials in the phantom. Deviations(Dev) between real and simulated date are listed as well.

Material	M(cm^{-1})	S(cm^{-1})	Dev(%)	σ_M(cm^{-1})	σ_S(cm^{-1})
$Ba(ClO_3)_2$	0.853	0.859	0.7	0.015	0.015
KBr	0.745	0.754	1.2	0.023	0.022
$CaCl_2$	0.748	0.720	3.9	0.021	0.023
$Pb(NO_3)_2$	0.769	0.776	0.9	0.022	0.022
PTA	0.776	0.777	0.1	0.021	0.020
H_2O	0.268	0.262	-2.2	0.026	0.022

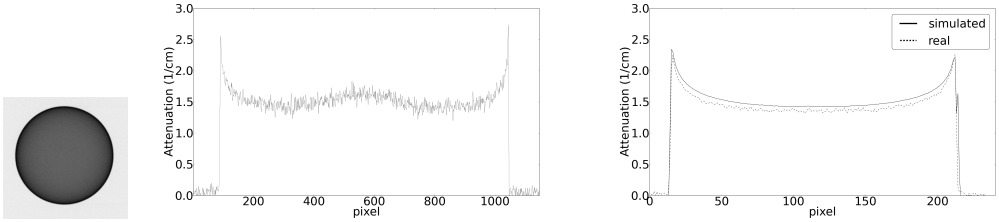

(a) (b) (c)

Figure 12: A reconstructed slice (a) of the real Al sphere and a line profile without (b) and with (c) the custom collimator. A line profile of a simulation taking only the photons emitted by the target into account, was added for comparison in (c).

shows a line profile of a real scan with the custom collimator compared with a simulation, where only the photons emitted by the target were taken into account. This profile shows a good agreement between both - a deviation of 5% was found - but again the difference is probably caused by the fact that the photons emitted by the secondary spot are not eliminated completely by the collimator.

4.4. Benchmarks

The simulations were performed on an ASUS GTX780-DC2OC-3GD5 GPU. Choosing a variable size for the energy bins as described in section 3.3 accelerates the computation time of a projection drastically. Together with the number of voxels in the phantom and the number of pixels of the detector these are the parameters that will influence the computation time for the projections. Table 5 gives the parameters used in the simulations described above and the computation time of a single projection and the full scan.

Table 5: Computation time for simulated projections and scans using a binned spectrum with 50 bins.

Parameter	Phantom	Al sphere
Phantom dimensions (x,y,z)	(365,365,40)	(1024,1024,100)
Detector dimensions (x,z)	(500,500)	(500,500)
number of projections	501	501
time for 1 projection (ms)	33	37
total simulation time (s)	16.6	18.6

4.5. Future improvements

Future improvements for the simulation program include a more generic way to generate different source and detector trajectories according to the needs of the user. Other implementations such as a finite spot size are still required because in the transmission tube described above a secondary spot produced by the Mo in the tube is present. Actual projection data also contains a contribution of previous images, also known as 'ghosting'. This effect is small and can have a magnitude of a few % (depending on the detector), but to improve the qualitative correctness of the simulations it should be included. The contribution is detector specific and originates in the detector 'panel'(aSi,...) and electronics and needs to be determined for

real detectors. Finally, the implementation of scattering and phase contrast would be a useful addition to the program.

5. Conclusion

A projection simulator has been developed at UGCT which allows a complete and realistic simulation of CT scans for a wide range of geometrical setups. In order to take into account the polychromatic behaviour of the X-ray tubes and detectors with great accuracy, extensive Monte Carlo simulations were performed. Using a ray-tracing technique and a voxel based approach for the sample, the radiographic projections are simulated.
A good agreement between real and simulated CT scans was demonstrated, with a maximum deviation between measured and simulated reconstructed attenuation coefficients of less than 4%. Consequently the simulation tool can be used to optimise scanning conditions in terms of scanning time, power, filtration and SNR for the scanners available at UGCT.

6. Acknowledgements

We acknowledge the Agency for Innovation by Science and Technology in Flanders (IWT, SBO project 120033 "TomFood") and the Special Research Fund of the Ghent University (BOF, GOA project 01G01008) for financial support.

References

[1] B. Masschaele, V. Cnudde, M. Dierick, P. Jacobs, L. Van Hoorebeke, and J. Vlassenbroeck. Ugct: new x-ray radiography and tomography facility. *Nucl. Instrum. Methods Phys. Res., Sect. A*, 580(1):266–269, 2007.

[2] B. Masschaele, M. Dierick, D. Van Loo, M. N. Boone, L. Brabant, E. Pauwels, V. Cnudde, and L. Van Hoorebeke. Hector: A 240kv micro-ct setup optimized for research. *J. Phys.: Conf. Ser.*, 463, 2013.

[3] M. Dierick, D. Van Loo, B. Masschaele, J. Van den Bulcke, J. Van Acker, V. Cnudde, and L. Van Hoorebeke. Recent micro-ct scanner developments at ugct. *Nucl. Instrum. Methods Phys. Res., Sect. B*, 324(0):35–40, 2014.

[4] J. A. Seibert and J. M. Boone. X-ray imaging physics for nuclear medicine technologists. part 2: X-ray interactions and image formation. *J. Nucl. Med. Technol.*, 33(1):3–18, 2005.

[5] P. Duvauchelle, N. Freud, V. Kaftandjian, and D. Babot. A computer code to simulate x-ray imaging techniques. *Nucl. Instrum. Methods Phys. Res., Sect. B*, 170(1-2):245–258, 2000.

[6] N. Freud, P. Duvauchelle, S. A. Pistrui-Maximean, J.-M. Ltang, and D. Babot. Deterministic simulation of first-order scattering in virtual x-ray imaging. *Nucl. Instrum. Methods Phys. Res., Sect. B*, 222(1-2):285–300, 2004.

[7] N. Freud, J.-M. Ltang, and D. Babot. A hybrid approach to simulate multiple photon scattering in x-ray imaging. *Nucl. Instrum. Methods Phys. Res., Sect. B*, 227(4):551–558, 2005.

[8] N. Freud, P. Duvauchelle, J.-M. Ltang, and D. Babot. Fast and robust ray casting algorithms for virtual x-ray imaging. *Nucl. Instrum. Methods Phys. Res., Sect. B*, 248(1):175–180, 2006.

[9] A. Peterzol, J. Berthier, P. Duvauchelle, C. Ferrero, and D. Babot. X-ray phase contrast image simulation. *Nucl. Instrum. Methods Phys. Res., Sect. B*, 254(2):307–318, 2007.

[10] D. Lazos, K. Bliznakova, Z. Kolitsi, and N. Pallikarakis. An integrated research tool for x-ray imaging simulation. *Comput. Methods Programs Biomed.*, 70(3):241–51, 2003.

[11] K. Bliznakova, Z. Kolitsi, and N. Pallikarakis. Dual-energy mammography: simulation studies. *Phys. Med. Biol.*, 51(18):4497–4515, 2006.

[12] K. Bliznakova, R. Speller, J. Horrocks, P. Liaparinos, Z. Kolitsi, and N. Pallikarakis. Experimental validation of a radiographic simulation code using breast phantom for x-ray imaging. *Comput. Biol. Med.*, 40(2):208–14, 2010.

[13] S. Kasperl, J. Hiller, and M. Krumm. Computed tomography metrology in industrial research and development. *Mater. Test.*, 51(6):405–411, 2009.

[14] F. Inanc. Scattering and its role in radiography simulations. *NDT E Int.*, 35(8):581–593, 2002.

[15] M. N. Boone, J. Vlassenbroeck, S. Peetermans, D. Van Loo, M. Dierick, and L. Van Hoorebeke. Secondary radiation in transmission-type x-ray tubes: Simulation, practical issues and solution in the context of x-ray microtomography. *Nucl. Instrum. Methods Phys. Res., Sect. A*, 661(1):7–12, 2012.

[16] R. Birch and M. Marshall. Computation of bremsstrahlung x-ray-spectra and comparison with spectra measured with a ge(li) detector. *Phys. Med. Biol.*, 24(3):505–517, 1979.

[17] D. M. Tucker, G. T. Barnes, and D. P. Chakraborty. Semiempirical model for generating tungsten target x-ray-spectra. *Med. Phys.*, 18(2):211–218, 1991.

[18] D. M. Tucker, G. T. Barnes, and X. Z. Wu. Molybdenum target x-ray-spectra: A semiempirical model. *Med. Phys.*, 18(3):402–407, 1991.

[19] J. M. Boone, T. R. Fewell, and R. J. Jennings. Molybdenum, rhodium, and tungsten anode spectral models using interpolating polynomials with application to mammography. *Med. Phys.*, 24(12):1863–74, 1997.

[20] G. Tirao, C. Quintana, F. Malano, and M. Valente. X-ray spectra by means of monte carlo simulations for imaging applications. *X-Ray Spectrom.*, 39(6):376–383, 2010.

[21] R. J. Mathar. Solid angle of a rectangular plate. `http://www.mpia-hd.mpg.de/~mathar/public/mathar20051002.pdf`, 2014.

[22] J. Vlassenbroeck, M. Dierick, B. Masschaele, V. Cnudde, L. Van Hoorebeke, and P. Jacobs. Software tools for quantification of x-ray microtomography at the ugct. *Nucl. Instrum. Methods Phys. Res., Sect. A*, 580(1):442–445, 2007.

[23] L. A. Feldkamp, L. C. Davis, and J. W. Kress. Practical cone-beam algorithm. *J. Opt. Soc. Am. A-Opt. Image Sci. Vis.*, 1(6):612–619, 1984.